MIMO Communication Measurements in Small Cell Scenarios at 28 GHz

Joerg Eisenbeis*, *Student Member, IEEE,* Magnus Tingulstad, Nicolai Kern, *Student Member, IEEE,* Zsolt Kollár, *Member, IEEE,* Jerzy Kowalewski, *Member, IEEE,* Pablo Ramos López, and Thomas Zwick, *Fellow, IEEE*

***Abstract*—Massive multiple-input multiple-output (MIMO) systems operating in the centimeter-wave (cmWave) and millimeter-wave (mmWave) region offer huge spectral efficiencies, which enable to satisfy the urgent need for higher data rates in mobile communication networks. However, the proper design of those massive MIMO systems first requires a deep understanding of the underlying wireless propagation channel. Therefore, we present a fully-digital MIMO measurement system operating around 28 GHz. The system enables to take fast subsequent snapshots of the complex MIMO channel matrix. Based on this method we statistically analyze the time-dependent channel behavior, the achievable signal quality and spectral efficiency, as well as the channel eigenvalue profile. Furthermore, the presented calibration approach for the receiver enables an estimation of the dominant absolute angle of arrival (AoA) and allows us to draw conclusions about the line-of-sight (LOS) dominance of the scenario. In total, 159 uplink communication measurements over 20 seconds are conducted in three different small cell site scenarios to investigate the wireless propagation behavior. The measurements reveal the existence of several spatial propagation paths between the mobile transmitter and the base station. Furthermore, an insight into their likelihood in different propagation scenarios is also given.**

***Index Terms*—Channel estimation, MIMO communication, Mobile communication**

I. Introduction

More than ever before, mobile wireless communication networks demand for higher data rates. To meet these requirements research and industry focus in particular on exploiting the large available spectral resources in the cmWave and mmWave region, the decrease of the the cell size to increase the spectral reuse, and the utilization of MIMO systems to achieve a spatial multiplexing gain [1]–[5]. As the path losses increase with higher carrier frequencies the application in mobile wireless communication networks is limited to small cell scenarios [6], [7]. Furthermore, at these higher frequencies massive MIMO mobile radio base stations, employing large-scale antenna arrays with hundreds of antenna elements, are realizable in a compact form factor, offering huge spectral efficiencies [8]–[10]. These huge spectral efficiencies are achieved by transmitting uncorrelated data streams to the spatially separated users and exploiting the multipath channel between the mobile radio base station and each user to obtain a spatial multiplexing gain [11]. As a result, the 3rd Generation Partnership Project (3GPP) lately defined the *n257*-band between 26.5 GHz - 29.5 GHz offering 3 GHz of spectral bandwidth [12].

To investigate the achievable data rates of massive MIMO communication systems in the *n257*-band and answer important system design questions, a deep understanding of the wireless propagation channel is required. Note that the propagation conditions determine the expected channel capacity of MIMO systems [13]. In practice, MIMO algorithms and architectures are evaluated in numerical simulations on the basis of models of the wireless propagation channel [14]. Nevertheless, these channel models depend on simplifications of the complicated electromagnetic propagation and thereby never fully reproduce the propagation effects [15]. For these reasons, extensive measurement campaigns have to be performed to characterize the wireless propagation channel and demonstrators are needed to verify the performance and validate channel models.

A. Channel Measurements around 28 GHz

Till date, many research groups realized channel sounding systems to investigate the propagation characteristics around 28 GHz as presented in [16]–[46]. Particularly worthy to mention are the extensive measurement campaigns by Rappaport et al. for the 28, 38, 60, and 73 GHz mmWave bands summarized in [16]. At 28 GHz the results for urban scenarios reveal path loss exponents of 2.1 for line-of-sight (LOS) and 3.4 for non-line-of-sight (NLOS) scenarios, which are similar to today's microwave path loss models [16], [47], [48].

Another important research aspect in wireless channel sounding is the analysis of the dynamic channel behavior. Therefore, the required measurement times to acquire the channel characteristics at each transmitter and receiver location have to be reduced. To better temporally analyze the wireless propagation channel Bas & Molisch et al. present in [17], [49] a MIMO channel sounder at 28 GHz based on a phased array structure that performs fast beam steering. Compared to channel sounders with rotating horn antennas

Manuscript received January 20, 2020; revised August 00, 2020. This work was supported by the Electronic Components and Systems for European Leadership (ECSEL) joint undertaking funded under H2020-EU.2.1.1.7. in frame of the TARANTO project with ID 737454 and the German Federal Ministry of Education under grant number 16ESE0211. Furthermore, the research reported in this paper has been supported by the Hungarian National Research, Development and Innovation Fund (TUDFO/51757/2019-ITM, Thematic Excellence Program).

During their work on this contribution all authors were with the Institute of Radio Frequency Engineering and Electronics (IHE), Karlsruhe Institute of Technology (KIT), 76131 Karlsruhe, Germany. Zsolt Kollár also is with the Budapest University of Technology and Economics, Hungary. E-mail: *joerg.eisenbeis@kit.edu.

the measurement time could drastically be reduced down to milliseconds [17]. The channel sounder is used to analyze the outdoor to indoor propagation channel in [50], [51] and to estimate the angular spectrum, delay spread, and Doppler spectrum in an outdoor micro cellular scenario in [52]. A different approach reducing the channel measurement time is introduced by Tataria & Tufvesson et al. in [19]. The presented MIMO channel sounder measures the 256×128 dual-polarized channel by switching between the different elements. In contrast to previous works, snapshots of the MIMO channel can be acquired in $380\,\mathrm{ms}$.

Beside the extensive channel characterization efforts made, first MIMO demonstrators operating within the *n257*-band have been presented in literature. Researchers from Samsung Electronics demonstrated in [53] first indoor and outdoor coverage tests using a subarray-based (sub-connected) hybrid beamforming testbed. This work was extended in [54] achieving data rates of up to $7.5\,\mathrm{Gbps}$ by transmitting four parallel data streams to two mobile stations in close distance. Recently, Yang et al. reported in [55] the first fully digital massive MIMO transceiver operating at $28\,\mathrm{GHz}$ consisting of 64 antenna elements. In the demonstrator test 20 non-coherent data streams could be transmitted at the same time to eight user entities resulting in a spectral efficiency of $101.5\,\mathrm{bps/Hz}$. Further MIMO communication measurements are presented by NTT Docomo in [56]–[58].

B. Main Contributions

To tackle the problem of long measurement times of current channel sounders and analyse achievable communication data rates within realistic small cell scenarios, we present a fully digital 16×4 MIMO measurement system operating around $28\,\mathrm{GHz}$. Unlike the channel sounders presented above, we analyze the wireless propagation behavior by estimating and evaluating subsequent snapshots of the complex MIMO channel matrix, representing the time-dependent channel response between each transmit and receive antenna assuming a frequency non-selective channel [59]. This method enables us to take snapshots of the channel in much less than a millisecond allowing a good analysis of the dynamic propagation behavior. The main contributions can be summarized as follows:

- This work presents a method to rapidly acquire narrowband snapshots of the complex MIMO channel matrix, which enables us to investigate the wireless propagation behavior around $28\,\mathrm{GHz}$.
- We verify this approach and analyze the MIMO wireless propagation channel in a total of 159 measurements in three different small cell site scenarios. For each measurement the mobile unit is placed at a different location and the received data is recorded for around $20\,\mathrm{s}$. Snapshots of the MIMO channel are estimated for each symbol, i.e. each $128\,\mu\mathrm{s}$.
- A calibration approach for fully digital MIMO architectures is presented and implemented at the receiver allowing the correction of amplitude and phase imbalances between the receive branches. This facilitates the estimation of the dominant absolute AoA. With simultaneous determination of the spatial positions of transmitter and receiver as well as the receiver orientation, the found AoA allows to draw conclusions about the LOS dominance of the scenario.
- We present for the first time measurement results for the channel eigenvalue statistics around $28\,\mathrm{GHz}$. This statistic reveals with which likelihood up to four spatial propagation paths can be utilized. Note that the eigenvalues of the channel determine if spatial multiplexing (Blast-type) communication techniques are wise to be applied [11].
- Furthermore, the subsequent snapshots of the MIMO channel matrix are used to evaluate the achievable spectral efficiencies. The measurement results give information about the degradation in spectral efficiency caused by foliage within the wireless propagation paths, as the coherence time is reduced.

It should be noted, that our MIMO communication demonstrator does not aim to replace current channel sounder, but rather serves as an complementary approach to analyze the so far insufficiently investigated channel characteristics, as for example the time-dependent eigenvalue profile of the channel. In advance the measured snapshots of the channel matrix can be directly fed into measurement-based MIMO channel models, to numerically analyze novel MIMO communication architectures and algorithms. Note that new architectures and algorithms are mostly evaluated in numerical simulations utilizing abstract MIMO channel models as presented in [60]–[64].

This work is organized as follows. Section II presents the hardware setup as well as the methods for receiver calibration and channel estimation. In section III the outdoor measurement scenarios are described in detail. Finally, section IV discusses the results of the channel analysis around $28\,\mathrm{GHz}$.

II. MIMO Channel Measurement Approach

To investigate the behavior of the wireless propagation channel around $28\,\mathrm{GHz}$ we developed a fully-digital MIMO measurement system. The system is designed to measure the multipath channel characteristic emulating an uplink communication scenario between a mobile user with $M_{\mathrm{ant}} = 4$ transmitters and a base station with $N_{\mathrm{ant}} = 16$ receivers. In this section we introduce the designed hardware setup and explain the developed channel estimation and system calibration approach. Furthermore, the estimation of the dominant AoA is explained and the modulation error ratio (MER) is discussed as a metric for assessing signal quality.

A. System Setup

The measurement system consists of a fully digital 16×4 MIMO configuration with 4 transmit antennas at the mobile user entity and 16 receive antennas at the base station. The block diagram of the system configuration is shown in Fig. 1. To achieve a high sensitivity, a heterodyne architecture is selected, which enables a flexible adjustment of the radio frequency (RF) and intermediate frequency (IF).

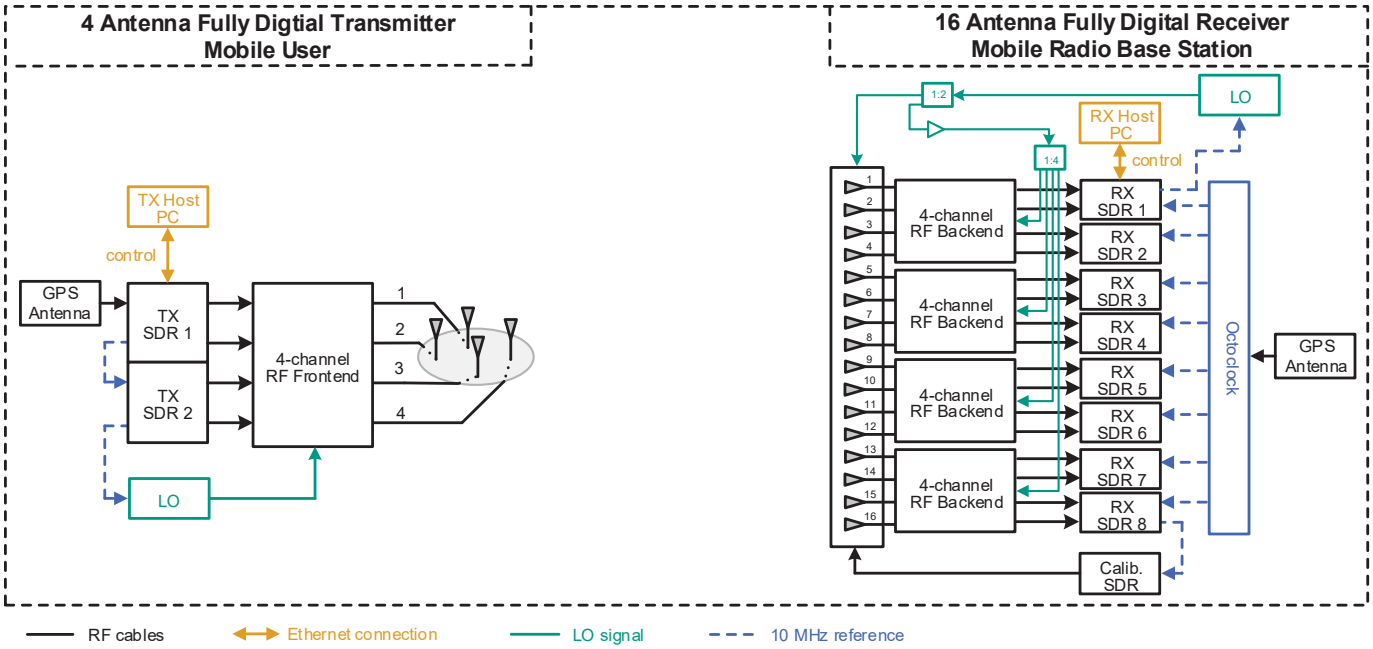

Fig. 1. Block diagram of the 16×4 MIMO channel sounder.

1) Mobile Transmitter: At the transmitter side the training signals for channel estimation are generated by a host computer (PC) connected via Gigabit-Ethernet to two commercial software defined radios (SDRs) of type *USRP X310* by *Ettus Research*. The SDRs include digital-to-analog-conversion (DAC), baseband to IF conversion, as well as IF filtering and amplification.

To translate the IF to the desired RF frequency band, a RF frontend with four symmetrical transmit branches is designed. It consists of a four metal layer printed circuit board (PCB) with a substrate of type *RO4003C* from *Rogers Corporation* with a height of $203\,\mu\mathrm{m}$ and a dielectric constant $\varepsilon_r = 3.55$. The IF-to-RF conversion and RF amplification is realized by commercially available monolithic microwave integrated circuits (MMICs). The PCB is integrated into a metallic housing for electromagnetic shielding, protection and better heat dissipation. The mixer includes an internal frequency doubler and the upper sideband of the mixing process is used, resulting in a RF center frequency

$$f_{\mathrm{RF}} = 2 f_{\mathrm{LO}} + f_{\mathrm{IF}}\,, \tag{1}$$

where f_{IF} is the IF in the range of $400\,\mathrm{MHz}$ to $3.5\,\mathrm{GHz}$ and f_{LO} is the externally supplied LO frequency in the range $12\,\mathrm{GHz}$ to $13.5\,\mathrm{GHz}$ depending on the selected IF. The RF can be set in the range of the *n257*-band between $26.5\,\mathrm{GHz}$ - $29.5\,\mathrm{GHz}$. For all inputs and outputs of the RF frontend module $2.92\,\mathrm{mm}$ connectors are utilized. The RF frontend is connected to the SDRs and the antenna via coaxial cables. The measured output $1\,\mathrm{dB}$-compression point of the RF frontend is $10\,\mathrm{dBm}$.

For the mobile transmitter four monopole antennas are mounted on a metallic housing to enable a $360°$ coverage in the azimuth plane. This makes the mobile transmitter independent of a rotation in azimuth. The monopole antennas have a height of $\lambda_0/4$ at $28\,\mathrm{GHz}$ to avoid dips in the elevation radiation pattern. In elevation the measured half power beamwidth (HPBW) is $26°$ with a main beam direction of $20.5°$ upwards originating from the ground plane of the monopoles. The tilt by $20.5°$ upwards is selected to be a good fit for the considered application scenario, where the base station is installed on a elevated position. The measured maximum realized element gain including connector and feed line losses is $1.5\,\mathrm{dBi}$. The monopoles are arranged in a square separated by $0.55\lambda_0$ at $28\,\mathrm{GHz}$ to achieve uniform coverage in azimuth over the entire $360°$ range. If the antennas are not properly spaced, notches in the azimuth radiation pattern would occur.

For the later measurement campaign the RF frontend and SDRs are integrated within a transportable box and placed together with the DC power supply and LO signal generator on a trolley shown in Fig. 2(c).

2) Base station: At the base station or receiver side a 16 antenna element board is designed with an element spacing of $5.35\,\mathrm{mm}$, which relates to a spacing of $\lambda_0/2$ at $28\,\mathrm{GHz}$. All antenna elements are realized as microstrip patch antennas using the same four metal layer *RO400C* PCB as for the RF frontend. To increase the antenna element gain two serially fed microstrip patch elements are vertically stacked, narrowing down the HPBW in elevation direction to $40.8°$. The HPBW in azimuth is $86°$. The measured realized element gain, including the connector and feed line losses, is $4.1\,\mathrm{dBi}$. A photo of the front of the antenna board is shown in Fig. 2(a).

The 16 RF outputs of the antenna board are connected via coaxial cables to four RF backends each consisting of four symmetric channels performing low noise amplification, bandpass filtering and RF-to-IF conversion. The RF backends are constructed according to the same scheme as for the RF frontends utilizing a four metal layer *RO400C* PCB, commercial available MMICs, $2.92\,\mathrm{mm}$ connectors and a

metal housing adapted to the PCB. Furthermore, the antenna board is mounted together with the RF backend modules onto a metallic construction, which allows a manual adjustment of the antenna elevation angle. The LO signal for RF-to-IF down-conversion is, similar to the transmitter side, supplied externally at half the mixing frequency to each RF frontend as shown in Fig. 1.

Finally, the received and digitized data is transferred via Ethernet to a host PC, where online and offline post-processing is performed. The receiver noise figure (NF) is calculated based on the information given in the data sheets of the used components to NF $\approx 2.1\,\mathrm{dB}$.

3) Transmitter and receiver clock and frequency synchronization: GPS-disciplined, oven controlled crystal oscillators (GPSDOs) by Ettus Research are employed to synchronize the SDRs and LO signal generators at the transmitter and receiver side. The GPSDOs provide a high-accuracy $10\,\mathrm{MHz}$ reference with phase noise of $-110\,\mathrm{dBc/Hz}$ at $10\,\mathrm{Hz}$ and a pulse-per-second (PPS) signal to ensure a synchronous sampling between the SDRs. At the transmitter the GPSDO is integrated into the first SDR. The $10\,\mathrm{MHz}$ reference and PPS is forwarded from the first SDR via daisy-chaining to the second SDR. Moreover the $10\,\mathrm{MHz}$ reference is provided to the LO signal generator as shown in Fig. 1. At the receiver the GPSDO is integrated into a *OctoClock-G CDA-2990* by *Ettus Research*. The *OctoClock-G CDA-2990* has eight $10\,\mathrm{MHz}$ reference and PPS outputs, which are connected to the SDRs at the receiver. The additional SDR for calibration receives the $10\,\mathrm{MHz}$ reference and PPS via daisy-chaining. Furthermore, the $10\,\mathrm{MHz}$ reference is forwarded by the first SDR via daisy-chaining to the LO signal generator at the receiver. The GPS coordinates provided in this process are also used in the later presented measurement campaigns to determine the spatial position of the transmitter and receiver.

B. Channel Estimation Principle and Signal Processing

To estimate the MIMO propagation channel, known training symbols are transmitted at the mobile user entity as it is standard in many communication systems [65], [66]. As signal waveform orthogonal frequency division multiplexing (OFDM) is used. The randomly selected training symbols are modulated using quadrature-phase shift keying (QPSK). OFDM facilitates the separation of the different transmit antennas by using exclusive OFDM subcarriers and enables the estimation of the complex MIMO channel matrix with several measurement points in the frequency domain [67]. By separating the transmit antennas in frequency domain, the transmitters can be separated at each receive antenna, realizing an estimation of the instantaneous complex MIMO channel matrix. The MIMO channel matrix represents the channel response between each transmit and receive antenna assuming a frequency non-selective channel [59]. To fulfill this assumption the signal bandwidth has to be smaller than the coherence bandwidth [68]. This also motivates to utilize OFDM, as the frequency-nonselectivity assumption just needs to be true for the bandwidth of a small range of OFDM subcarriers.

Let $\mathcal{I} \in \{0, 1, \ldots, N_c - 1\}$ be an index set addressing the N_c OFDM subcarriers and divide it into a subset of indices $\mathcal{I}_d$, containing the complex modulated data symbols used for channel estimation purposes and a subset of indices $\mathcal{I}_0$, containing the positions of all null carriers. It holds

$$\mathcal{I}_d \,\dot\cup\, \mathcal{I}_0 = \mathcal{I}\,. \tag{2}$$

Furthermore, the subset $\mathcal{I}_0$ contains the indices of the subcarriers around zero frequency to avoid blockage due to high DC parts $\mathcal{I}_{\mathrm{DC}} \subseteq \mathcal{I}_0$, the indices of upper and lower guard carriers $\mathcal{I}_{\mathrm{guard}} \subseteq \mathcal{I}_0$, and further recessed OFDM subcarriers for receiver calibration $\mathcal{I}_{\mathrm{cal}} \subseteq \mathcal{I}_0$. Hence, no subcarrier index is part of two subsets meaning the sets are disjoint so that

$$\mathcal{I}_0 = \mathcal{I}_{\mathrm{DC}} \cup \mathcal{I}_{\mathrm{guard}} \cup \mathcal{I}_{\mathrm{cal}} \tag{3}$$

and

$$\mathcal{I}_{\mathrm{DC}} \cap \mathcal{I}_{\mathrm{guard}} \cap \mathcal{I}_{\mathrm{cal}} = \emptyset \tag{4}$$

is fulfilled. The transmit antennas are separated for the channel estimation process using exclusive OFDM subcarriers. Therefore, the index set $\mathcal{I}_d$ is divided into M_{ant} subsets $\mathcal{I}_{d,m} \subseteq \mathcal{I}_d$ with $m \in \{1, 2, \ldots, M_{\mathrm{ant}}\}$ containing the $|\mathcal{I}_{d,m}|$ exclusive subcarriers of the m-th transmit antenna. It holds

$$\mathcal{I}_d = \dot{\bigcup_{m=1}^{M_{\mathrm{ant}}}} \mathcal{I}_{d,m}\,. \tag{5}$$

The OFDM subcarrier indices follow an interleaved assignment to the different transmit antennas to minimize the spacing between two neighboring subcarriers of one subset $\mathcal{I}_{d,m}$. The OFDM subcarrier spacing is defined as

$$\Delta f = B_s / N_c = 1/T_{\mathrm{o}} \tag{6}$$

where B_s represents the available signal bandwidth and T_{o} the OFDM symbol duration.

Based on the defined index sets the complex OFDM data frame for one OFDM symbol in the frequency domain $\boldsymbol{X} \in \mathbb{C}^{M_{\mathrm{ant}} \times N_c}$ is constructed. The discrete OFDM time domain signal with sampling time $t = q \cdot T_{\mathrm{o}}/N_c$ and $q \in \{0, 1, \ldots, N_c - 1\}$ can be written as [59], [69]

$$\boldsymbol{u}(m, q) = \sum_{p=0}^{N_c - 1} \boldsymbol{X}(m, p) \cdot e^{j 2\pi p q / N_c}\,, \tag{7}$$

where $p \in \{0, 1, \ldots, N_c - 1\}$ denotes the indices for the OFDM subcarrier frequencies $f_p = p \cdot \Delta f = p/T_{\mathrm{o}}$. The channel response of a multipath channel can be represented by [70], [71]

$$\boldsymbol{h}(n, m, q) = \sum_{d=0}^{N_p - 1} \boldsymbol{h}_c(n, m, d, q) \cdot \delta(q - d) \tag{8}$$

consisting of N_p replicas of the transmit signal arriving with the discrete delay time in samples d and complex weighting factor $\boldsymbol{h}_c(n, m, d, q)$ at the time sample point q at the receiver. For the received signal follows with the index set $n \in \{0, 1, \cdots, N_{\mathrm{ant}} - 1\}$ of the receive antennas

$$\begin{aligned} &\boldsymbol{y}(n, q) \\ &= \sum_{m=0}^{M_{\mathrm{ant}} - 1} \sum_{d=0}^{N_p - 1} \boldsymbol{h}_c(n, m, d, q) \cdot \boldsymbol{u}(m, q - d) + \boldsymbol{n}(n, q)\,, \end{aligned} \tag{9}$$

(a) Close-up photo of the base station setup in the cell site scenario II.

(b) View of the base station from the user's perspective.

(c) Mobile transmitter setup as seen from the base station.

Fig. 2. Photos of the base station and mobile transmitter setup.

where $\boldsymbol{n} \in \mathbb{C}^{N_{\text{ant}} \times N_c}$ accounts for the additive white Gaussian noise introduced during transmission. The multiplication of the transmit signals with a time-variant channel would lead to a cyclic convolution in frequency domain and thereby to inter-carrier-interferences (ICI). To avoid ICI the OFDM symbol duration has to be chosen smaller than the coherence time of the channel, so that the complex channel coefficients $\boldsymbol{h}_c(n, m, d, q)$ can be assumed constant over one OFDM symbol. With this assumption the received signal in the frequency or symbol domain results after discrete Fourier transformation (DFT) to

$$\begin{aligned}&\boldsymbol{R}(n,p)\\ &= \sum_{m=0}^{M_{\text{ant}}-1} \sum_{d=0}^{N_p-1} \text{DFT}\{\boldsymbol{H}(n,m,d) \cdot \boldsymbol{u}(m,q-d)\} + \boldsymbol{N}(n,p)\,.\end{aligned} \tag{10}$$

To avoid inter-symbol-interferences (ISI), the same OFDM symbol is transmitted continuously, thereby omitting the need for a guard interval. Due to the cyclic properties of the transmit sequence the time shifting property of the DFT

$$\boldsymbol{u}(\cdot, q-d) \circ\!\!-\!\!\bullet\, \boldsymbol{X}(\cdot,p) \cdot e^{-j2\pi qd/N_c} \tag{11}$$

can be exploited, leading to

$$\begin{aligned}&\boldsymbol{R}(n,p)\\ &= \sum_{m=0}^{M_{\text{ant}}-1} \sum_{d=0}^{N_p-1} \boldsymbol{H}(n,m,d)\boldsymbol{X}(m,p)e^{-j2\pi pd/N_c} + \boldsymbol{N}(n,p)\,,\\ &= \sum_{m=0}^{M_{\text{ant}}-1} \tilde{\boldsymbol{H}}(n,m)\boldsymbol{X}(m,p) + \boldsymbol{N}(n,p)\,,\end{aligned} \tag{12}$$

with the channel frequency response

$$\tilde{\boldsymbol{H}}(n,m) = \sum_{d=0}^{N_p-1} \boldsymbol{H}(n,m,d)e^{-j2\pi pd/N_c}\,. \tag{13}$$

At the receiver the channel can be estimated using least squares estimation [72]

$$\hat{\boldsymbol{H}}_{\text{f}}(n,p) = \boldsymbol{R}(n,p) \cdot \boldsymbol{T}(p)^{-1} \tag{14}$$

with the known transmit data symbols

$$\boldsymbol{T}(p) = \sum_{m=0}^{M_{\text{ant}}-1} \boldsymbol{X}(m,p)\,. \tag{15}$$

As the transmitters are separated by their OFDM subcarriers defined in $\mathcal{I}_{d,m}$ the MIMO channel matrix can be estimated to

$$\hat{\boldsymbol{H}}(n,m) = \frac{1}{|\mathcal{I}_{d,m}|} \sum_{p \in \mathcal{I}_{d,m}} \hat{\boldsymbol{H}}_{\text{f}}(n,p) \tag{16}$$

averaging over all subcarrier of each transmitter assuming a frequency non-selective channel for the full signal bandwidth $B_s = N_c \cdot \Delta f$. It is therefore necessary that the receiver knows the training symbols as well as the OFDM subcarrier indices of the individual transmitters $\mathcal{I}_{d,m} \forall m$.

C. System Calibration and AoA Estimation

An important achievement of the hardware design is the determination of the strongest absolute AoA at the receiver. This requires a correction of the imbalances in amplitude and phase between the 16 RF receive branches, which result from cable length deviations, manufacturing tolerances of the PCBs and MMICs, deviations in soldering, and phase differences of the LO signals. Especially the used SDRs cause a random phase offset between the branches because there is no possibility to harmonize the phase of the LO signals for IF up- and down-conversion. Therefore, a calibration branch was added to the hardware design to correct these imbalances. The calibration branch consists of an additional SDR at the receiver generating the calibration signal, which is fed at the IF to a dedicated input port of the receiver antenna board. The receiver antenna board incorporates a mixer which up-converts the calibration signal to RF by means of an externally

supplied LO signal at half the mixing frequency as shown in Fig. 1. The calibration signal is then split symmetrically by a distribution network and added to the receive signal directly behind the 16 antenna elements using a coupled line directional coupler. As the calibration signal is known at the receiver and is symmetrically coupled into each receive path, the relative differences between the amplification and phase of the receive branches can be estimated and corrected in the digital domain of the receiver. The amplitude and phase imbalances have to be only corrected with respect to a selected receiver branch. It is important to mention that to enable a real-time calibration the received and calibration signals have to be separated to avoid interference. This separation is achieved by keeping selected OFDM carriers of the transmitted signal free for the calibration signal. As defined before the OFDM subcarrier calibration index set is denoted by $\mathcal{I}_{\text{cal}}$ and it holds $\mathcal{I}_{\text{cal}} \cap \mathcal{I}_d = \emptyset$. The introduced imbalances are measured for each OFDM symbol in the same manner as in (14) resulting to

$$\hat{d}_n = \frac{1}{|\mathcal{I}_{\text{cal}}|} \sum_{p \in \mathcal{I}_{\text{cal}}} \tilde{\boldsymbol{R}}(n,p) \cdot \boldsymbol{C}(n)^{-1}, \tag{17}$$

where $\tilde{\boldsymbol{R}}$ represents the received baseband signal matrix including the superimposed calibration signal. Finally, the result is used to obtain the calibrated MIMO channel matrix

$$\hat{\boldsymbol{H}}_{\text{cal}} = \hat{\boldsymbol{D}}^{-1} \cdot \hat{\boldsymbol{H}} \tag{18}$$

with the calibration matrix $\hat{\boldsymbol{D}} = \text{diag}\{\hat{d}_0, \cdots, \hat{d}_{N_{\text{ant}}-1}\}$.

Based on the calibrated channel matrix, the strongest AoA $\hat{\phi}_{\text{max}}$ can be determined. Therefore the singular value decomposition (SVD) of the calibrated channel matrix is calculated $\hat{\boldsymbol{H}}_{\text{cal}} = \hat{\boldsymbol{U}}\hat{\boldsymbol{\Sigma}}\hat{\boldsymbol{V}}^H$ to extract the first receiver side beamforming vector $\hat{\boldsymbol{u}}_1 \in \mathbb{C}^{N_{\text{ant}} \times 1}$ of $\hat{\boldsymbol{U}} = [\hat{\boldsymbol{u}}_1^T, \ldots, \hat{\boldsymbol{u}}_{N_{\text{ant}}}^T]^T$. The radiation pattern over the azimuth angle ϕ using the first receiver side beamforming vector results to

$$\boldsymbol{C}(\phi) = \sum_{n=0}^{N_{\text{ant}}-1} \hat{\boldsymbol{u}}_1^H(n) \boldsymbol{C}_{\text{e}}(n,\phi) e^{jk\boldsymbol{d}(n)\sin\phi}, \tag{19}$$

where $\hat{\boldsymbol{u}}_1^H$ denotes the Hermitian transpose of $\hat{\boldsymbol{u}}_1$, $\boldsymbol{C}_{\text{e}}$ contains the antenna element characteristics, $k = 2\pi/\lambda$ denotes the wave number, and $\vec{d}$ represents a vector with the spatial positions of the active antenna elements. As the first receiver side beamforming vector enables a beam steering into the direction of the strongest AoA the corresponding angle can be extracted by finding the maximum in the radiation pattern. The strongest AoA is therefore given by

$$\hat{\phi}_{\text{max}} = \arg\max_{\phi} \{|\boldsymbol{C}(\phi)|\}, \tag{20}$$

which can be compared with the physical azimuth angle between the position of the base station and the mobile transmitter ϕ_{bt}. The angle ϕ_{bt} can be calculated using the GPS coordinates of the base station and the mobile transmitter with respect to the view direction of the base station. The angular difference

$$\Delta\phi = |\phi_{\text{bt}} - \hat{\phi}_{\text{max}}| \tag{21}$$

equals zero for scenarios with a dominant LOS path but can have an arbitrary value for NLOS scenarios. This means that the angular difference $\Delta\phi$ can give information about whether the scenario is LOS dominated. In principle, multiple AoAs can be extracted from the estimated and calibrated channel matrix, by analyzing the radiation characteristic including all beamforming vectors given by $\hat{\boldsymbol{U}}^H$.

D. Signal Quality and Performance Metrics

As a measure of the signal quality, the MER representing a quasi SNR is calculated. Before estimating the MER the received symbols are equalized assuming a frame based data transmission with frame length L_{f} with periodic appearing training symbols as it is common practice in wireless communications [73]. A one tap equalization is applied using as an equalization matrix

$$\boldsymbol{\Lambda} = \frac{1}{L_{\text{f}}} \sum_{k=0}^{L_{\text{f}}-1} \hat{\boldsymbol{H}}_{\text{f}}(\cdot,\cdot,k) \tag{22}$$

where $\hat{\boldsymbol{H}}_{\text{f}} \in \mathbb{C}^{N_{\text{ant}} \times N_c \times L_{\text{f}}}$ is the result of (14) extended in time domain with sampling times $t = k \cdot T_{\text{o}}$ for $k \in \{0, 1, \ldots, L_{\text{f}} - 1\}$. On the basis of the equalized receive symbols $\boldsymbol{R}_{\text{eq}} \in \mathbb{C}^{N_{\text{ant}} \times N_c \times L_{\text{f}}}$ the MER averaged over all receivers and all OFDM carriers is defined by

$$\text{MER} = 10 \cdot \log_{10} \left\{ \frac{\sum_{p=0}^{N_c-1} \boldsymbol{P}_{\text{ref}}(p)}{\sum_{n=1}^{N_{\text{ant}}} \sum_{p=0}^{N_c-1} \sum_{k=0}^{L_{\text{f}}-1} \boldsymbol{E}(n,p,k)} \right\} \tag{23}$$

with the error matrix

$$\begin{aligned} \boldsymbol{E}(n,p,k) = &[\text{Re}\{\boldsymbol{T}(p)\} - \text{Re}\{\boldsymbol{R}_{\text{eq}}(n,p,k)\}]^2 \\ &+ [\text{Im}\{\boldsymbol{T}(p)\} - \text{Im}\{\boldsymbol{R}_{\text{eq}}(n,p,k)\}]^2 \end{aligned} \tag{24}$$

and the normalization matrix

$$\boldsymbol{P}_{\text{ref}}(p) = \text{Re}\{\boldsymbol{T}(p)\}^2 + \text{Im}\{\boldsymbol{T}(p)\}^2 \tag{25}$$

following the descriptions in [74]. Furthermore, the MER can be averaged over $L_s = \lfloor L_{\text{tot}}/L_{\text{f}} \rfloor$ subsequent OFDM frames, where L_{tot} represents the total number of recorded OFDM symbols.

As a performance metric serves the spectral efficiency or maximum achievable sum rate given in bps/Hz and calculated by [75]

$$R = \log_2 \left\{ \left| \boldsymbol{I}_{N_{\text{ant}}} + \frac{\gamma}{M_{\text{ant}}} \hat{\boldsymbol{H}} \hat{\boldsymbol{H}}^H \right| \right\} \tag{26}$$

with the normalized channel matrix $||\hat{\boldsymbol{H}}||^2 = N_{\text{ant}} M_{\text{ant}}$. For the SNR at the receiver γ we use the calculated MER in the following analysis.

III. Outdoor Measurement Scenarios

For the channel measurements we selected three different cell site scenarios to obtain a realistic picture of the wireless propagation channel. The scenarios were chosen due to their variability in foliage coverage, reflective surfaces, denseness of buildings, availability of LOS and NLOS measurement points

and their angular spread. Within each scenario we positioned the base station at an elevated position with a fixed view direction and elevation angle. The position of the mobile transmitter is varied within a pre-designated measurement area seen from the base station view direction, making an analysis of the different propagation scenarios and view angles to the base station possible. The determination of the exact spatial position of the transmitter and receiver is based on the recorded and over the measurement period averaged GPS data which are manually verified using a map of the scenario. The position deviation is therefore estimated to be less than 2 m. For each measurement position of the mobile transmitter an around 20 s long recording is made. This allows us to analyze the time dependent behavior of the channel, as for example the influence of foliage movement within the propagation paths. In total 159 measurements are performed and evaluated.

The measurements are performed on several days from May to July causing a high amount of foliage within the surrounding area. During the measurements the weather was partly cloudy and dry. Three different small cell site scenarios were picked for comparison at Campus South of the Karlsruhe Institute of Technology (KIT). For each cell site scenario the elevation and azimuth view direction of the base station is adjusted upfront to cover the desired area best possible. The scenarios are marked in the satellite image in Fig. 3. The image shows the respective position of the base station (B_1, B_2, and B_3), their view directions[1] and the angular ranges of $\pm 60°$ around the view directions. The different cell sites can be described as follows:

1) Scenario I: In the first scenario the base station is adjusted to cover an open courtyard, which is characterized by a small lake surrounded by buildings on its three sides serving as possible reflective surfaces. Furthermore, a fair amount of foliage belonging to tall trees in the center of the courtyard was present. These blocked a direct LOS propagation between base station and the mobile transmitter at some of the measurement locations, which shows a significant impact on the signal-to-noise ratio (SNR). At the furthermost end of the courtyard, two small building-canyons run on either side of a building, possibly creating highly reflective environments. Additionally, some parked cars prevented the direct LOS path. The base station is positioned on the balcony of an adjacent building in 13 m height and the antenna array is tilted downwards in elevation by 12° from the horizontal view direction.

2) Scenario II: The second scenario covers an intersection and is dominated by heavy foliage spread over a wide angular range, as shown on the right side of the satellite image in Fig. 3. The base station is thereby placed on the roof top of a building in 17 m height and tilted in elevation by 15° downwards from the horizontal view direction. The heavy foliage coverage, is blocking the LOS path at multiple measurement locations, giving possibility to further investigate the influences of foliage onto the propagation channel. Compared to the first cell site scenario, a less reflective environment is present, with a wide street running through the scenario lined by trees and parked cars. Furthermore, occasional wind present on the day of measurement introduced time-variant scattering effects due to movements of the foliage during the measurement times.

3) Scenario III: In the third scenario the base station is placed on a balcony in 35 m height and the antenna array is tilted downwards in elevation by 28° from the horizontal view direction. This scenario comprises few trees, which in combination with the base station height is leading to measurement distances up to 162 m. Here, urban NLOS propagation scenarios are present at several measurement locations.

The key figures of the different cell site scenarios are summarized in Tab. I. To enable a realistic mobile communication scenario, the antennas of the mobile transmitter are placed at a height of 115 cm in all scenarios to emulate the typical height of a cell phone carried by a user. Moreover, the height of the base stations are chosen following the urban micro and macro cell scenarios with high user density identified by 3GPP in [76]. Due to a maximum distance of 162 m within the measurements, the atmospheric gap around 28 GHz and the absence of rain during our measurements, the additional atmospheric path losses can be neglected [77].

TABLE I
OVERVIEW OF THE CELL SITE PARAMETERS.

	Scenario I	Scenario II	Scenario III
Base station height	13 m	17 m	35 m
Tilt in elevation	12°	15°	28°
No. of measurements	49	62	48
Min. distance	28 m	22 m	49 m
Max. distance	99 m	124 m	162 m
Max. azimuth angle	64.5°	92.1°	61.4°

IV. Channel Measurement Results

In the following section the results of the channel measurements are presented. The system parameters used for our measurements are given in Tab. II. The considerably narrow bandwidth is selected to ensure a frequency-nonselective channel behavior. It should be noted, that the presented measurements focus on estimating snapshots of the complex MIMO channel matrix. For more information about the broadband channel behavior or other characteristics as for example power delay profiles we refer to the measurement results presented in [16], [18], [50], [52], [78]. Nevertheless, it is generally possible to use the demonstrator for broadband channel measurements as the designed RF frontends cover the full *n257*-band. For this purpose, the IF frequency can be varied in time by controlling the utilized SDRs and thus a wide frequency range can be investigated. However, this presupposes a stationary channel over the entire measurement. The modular design also allows the replacement of the bandwidth limiting antennas and SDRs by analog-to-digital converter (ADC) and digital-to-analog converter (DAC) boards with higher sampling rates and processing speeds.

At first, the average MER over the full recording is calculated for each transmitter position and color-coded displayed

[1] normal vector to the antenna array plane

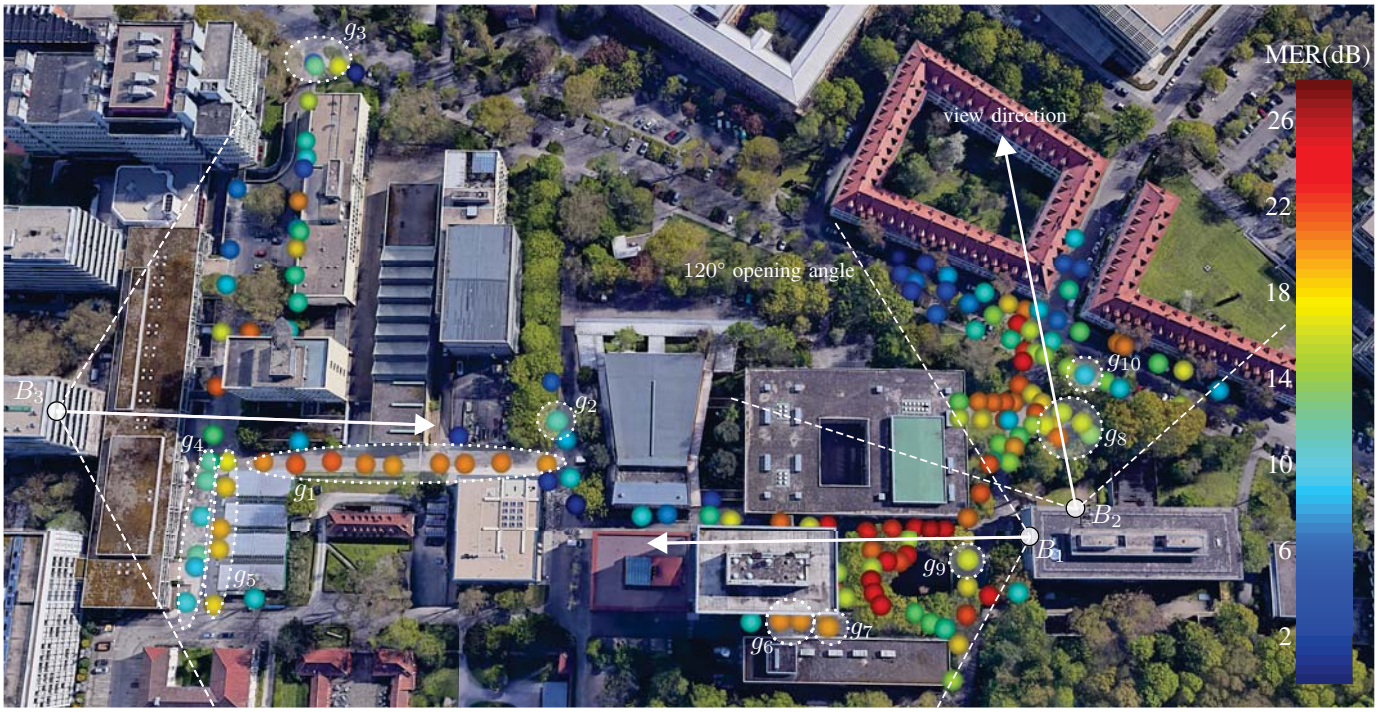

Fig. 3. Satellite image of the measurement cell site scenarios at KIT Campus South. For the base station positions (B_1,B_2,B_3) marked as white circles, the view direction of the antenna array as well as an azimuth opening angle of 120° is drawn into the picture. Furthermore, the estimated average MER over the whole recording is color-encoded shown for each position of the mobile transmitter. The cell site scenarios cover LOS as well as NLOS scenarios, azimuth angles of over 60° and distances up to 162 m. The measurements reveal the suitability of buildings as reflectors and the influence of vegetation onto the measurements. For better reference parts of the measurement locations are grouped by semitransparent white dashed lines and indexed as $\{g_1, g_2 \cdots, g_{10}\}$. *Image source: Google Earth 2019 GeoBasis-DE/BKG.*

TABLE II
MEASUREMENT SYSTEM PARAMETERS.

Parameter	Symbol	Value
MIMO size	$N_{\text{ant}} \times M_{\text{ant}}$	16×4
RF frequency	f_{RF}	27.8 GHz
IF	f_{IF}	2.46 GHz
Transmit power	P_{Tx}	10 dBm
Tx antenna element gain	G_{Tx}	1.5 dBi
Rx antenna element gain	G_{Rx}	4.1 dBi
Estimated receiver noise figure	NF	2.1 dB
Sampling frequency	f_s	1 MSps
Frame length	L_{f}	10
FFT size	N_c	128 points
OFDM subcarrier spacing	$\Delta f = f_s/N_c$	7.8125 kHz
Number of allocated carriers	$\lvert\mathcal{I}_d\rvert$	80
Number of calibration carriers	$\lvert\mathcal{I}_{\text{cal}}\rvert$	10
Number of DC null carriers	$\lvert\mathcal{I}_{\text{DC}}\rvert$	5
Number of guard carriers	$\lvert\mathcal{I}_{\text{guard}}\rvert$	33
OFDM symbol duration	T_{o}	128 µs
Digital modulation scheme		QPSK

into Fig. 3. The results show that the MER varies strongly depending on the position of the mobile transmitter. This is caused by the high number of trees in the propagation paths, which lead to large path losses at 28 GHz. For good propagation scenarios MER values of up to 26 dB could be reached. These values are achieved without using any antenna array gain, i.e. an EIRP of 11.5 dBm, due to the employed channel estimation technique. The MER values therefore look quite promising for future 28 GHz MIMO mobile communication systems. As expected, the highest values could be reached in short distance LOS scenarios at or close to the view direction of the base station. The group of measurement locations marked as g_1 in Fig. 3 shows multiple LOS measurements with different distances between the base station and the mobile transmitter ranging from 64 m to 150 m. The elevation angle decreases thereby from 33° to 13° the further the transmitter moves away from the base station. The measurements show that the MER only slightly decreases with distance, as a lower elevation angle between the base station and the mobile transmitter leads to a higher antenna element gain at the transmitter and receiver side. Moreover, foliage losses can be estimated using the furthermost point of g_1 and comparing it with the measurement position of g_2. Note that a slight difference in distance for both locations has only a minor impact on the path loss and thereby MER. The measurements show a difference in MER of 9.5 dB due to foliage in the LOS path. Measurement group g_3 indicates that the MIMO system can successfully operate within a high angular range in azimuth of above 60° achieving MER values of up to 17 dB. The measurement positions summarized in g_4 have no direct LOS connection to the base station, as the

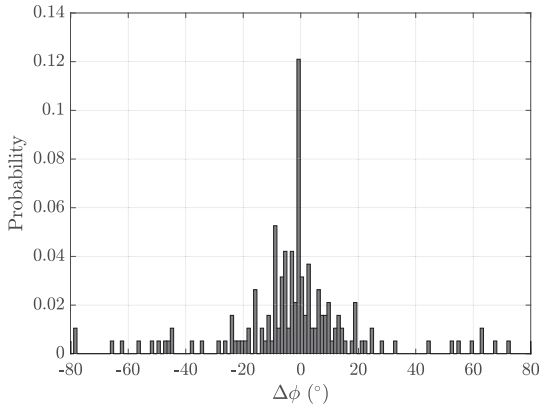

Fig. 4. Statistic of the angular difference $\Delta\phi$ between the physical azimuth angle and the main azimuth beam direction over all mobile transmitter positions in all three cell site scenarios.

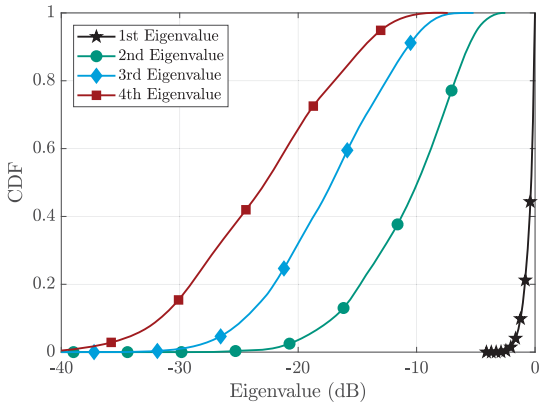

Fig. 5. Cumulative distribution function of the normalized eigenvalues of the channel including all mobile transmitter locations of all cell site scenarios.

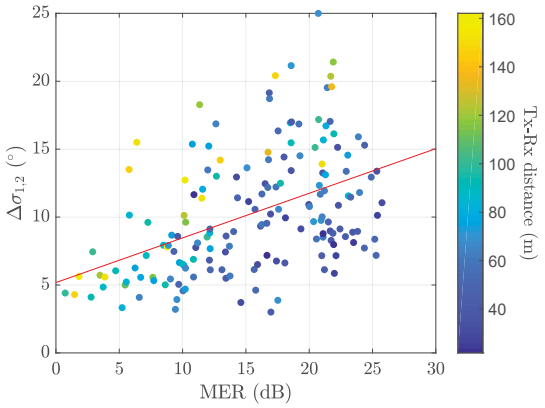

Fig. 6. Difference between the first and second eigenvalue of the channel $\Delta\sigma_{1,2}$ versus the average MER. The distance between the base station receiver and the mobile transmitter is color-encoded into the graph.

mobile transmitter was shadowed by the adjacent building. Interesting is the comparison with the measurement positions in g_5 made on the other side of the street enabling a LOS connection. The difference in MER between both groups is roughly $8.5\,\mathrm{dB}$, showing the stronger path loss of NLOS propagation scenarios. Nevertheless, the difference in MER in the NLOS connection of measurement position g_6 and the LOS connection of measurement position g_7 is only $0.2\,\mathrm{dB}$. This low loss in the NLOS case results from high building fronts surrounding the mobile transmitter like a canyon, which enables the propagation towards the base station. The high influence of the vegetation like trees and bushes onto the path loss can be shown in group g_8, where a high number of spatially close measurements have been made showing a high range of MER values varying between $16\,\mathrm{dB}$ and $22\,\mathrm{dB}$.

To analyze if the wireless propagation channel is LOS or NLOS dominant the histogram of the angular difference $\Delta\phi$ calculated by (21) is depicted in Fig. 4 including all mobile transmitter positions. The result shows a LOS dominance within the measurements made. The reasons for this are not only the selection of the mobile transmitter locations, but also the fact that the likelihood for multipath propagation decreases compared to frequencies below $6\,\mathrm{GHz}$. This is caused by the higher path losses and absorption by possible reflectors. Besides the peak around $\Delta\phi = 0°$ the angular difference is spread over the whole range. Note that due to the limited number of measurements not every angular difference is present in Fig. 4.

To analyze the multipath nature of the wireless propagation channel in detail Fig. 5 provides the cumulative distribution function (CDF) of the four eigenvalues of the channel including all mobile transmitter locations of all cell site scenarios. The graph reveals the multipath nature of the wireless propagation channel. It can be seen, that even in this LOS dominated cell site scenarios in $50\,\%$ of the cases the second eigenvalue is not more than $10\,\mathrm{dB}$ lower than the strongest one. Moreover, in $10\,\%$ of the cases the difference between the strongest and weakest eigenvalue is less than $14\,\mathrm{dB}$.

For a deeper understanding of the multipath behavior of the $28\,\mathrm{GHz}$ propagation channel, taking a closer look at the difference between the first and second eigenvalue $\Delta\sigma_{1,2}$ is of interest. In Fig. 6 the eigenvalue difference is plotted over the MER for all locations of the mobile transmitter. The eigenvalue difference is averaged in time over the full recording. Furthermore, the distance between the base station and mobile transmitter is color-encoded onto the measurement points. Fig. 6 shows that for low MER values the differences between the first and second eigenvalues of the channel are low. This can be explained by the type of scenario causing the low MER. These scenarios mostly have no LOS connection and the distance between the base station and mobile transmitter is comparably high, as shown by the color-encoded points. Hence, if no dominant path exists, the difference between the eigenvalues most likely decreases. Going to higher MER values the difference in the eigenvalues seem to increase in average as indicated by the trend line. This is mainly caused by LOS scenarios, as reflections over e.g. buildings are much higher attenuated compared to the direct path. At medium to high values of the MER, all distances are represented supporting the thesis of LOS dominance. Furthermore the results reveal that at medium and high MER values the distance between the eigenvalues decreases predominantly if the distance between the base station and mobile transmitter is low. This means that at closer distances multipath scenarios

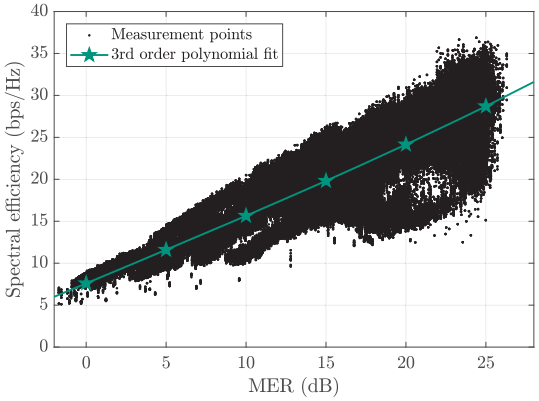

Fig. 7. Statistic of the achievable spectral efficiency versus the average MER for all mobile transmitter measurement locations of all cell site scenarios. The tendency of the measured spectral efficiency is illustrated using a third order polynomial.

exist, which can be exploited for spatial multiplexing or diversity transmission.

To investigate the achievable spectral efficiency in the presented mobile communication scenarios, the spectral efficiency for all mobile transmitter positions and all scenarios is depicted in Fig. 7. Additionally the course of the spectral efficiency is approximated as a third order polynomial function using the measurement data. While the spectral efficiency increases with an increasing MER, the uncertainty also rises. This behavior is in line with the observations made in Fig. 6. For high MER values the scenario may have only one dominant LOS path leading to a low spectral efficiency, as only the first eigenvalue contributes to the transmission. The spectral efficiency in this case is dominated by the eigenvalue distribution. At low MER values all eigenvalues are highly attenuated, which means that the spectral efficiency is dominated by the MER. As for wider bandwidths additional frequency selective distortions will reduce the signal quality, the presented results of the narrowband achievable spectral efficiency can be used as an indicator for the reachable performance. This helps designers of broadband communication systems to put the achieved spectral efficiency into perspective and indicates the amount of additional interference caused by broadband data transmission.

Next, the time-dependent behavior of the propagation channel is analyzed. For this the beamforming matrices resulting from SVD may be applied to time delayed instances of the channel matrix. Note that in real communication scenarios the channel estimate is used during the transmission of the full frame until the channel estimation is updated, utilizing non-continuous channel estimation approaches. This processing is valid as long as the coherence time is much larger than the frame duration or channel estimation update time. To evaluate the time-dependent behavior, the CDF of the spectral efficiency is calculated for a slow changing and fast changing environment shown in Fig. 8. In each case different frame durations given in multiples of the OFDM symbol duration are used. Note that as the channel is changing, the employed outdated beamforming matrix could also lead to an improvement in spectral efficiency. This is caused by a

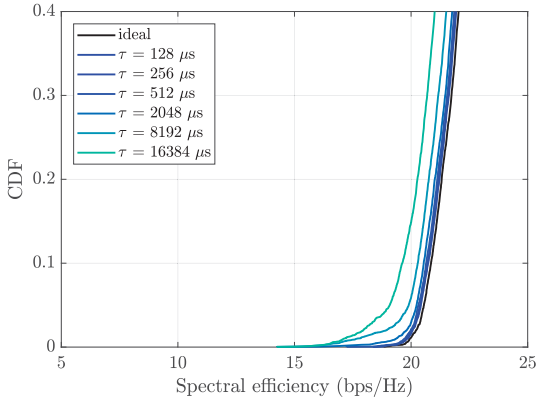

(a) Measurement location marked as g_9 within Fig. 3 showing a slow changing wireless propagation channel meaning a long coherence time.

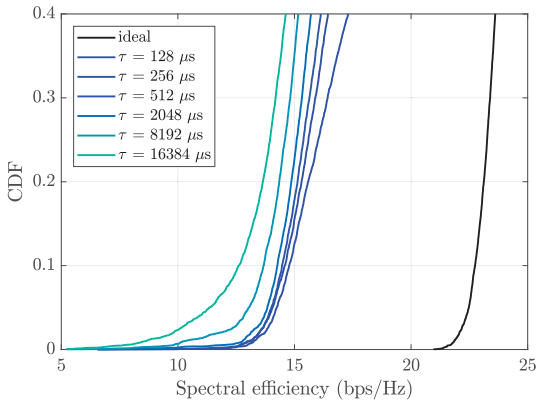

(b) Measurement location marked as g_{10} within Fig. 3 showing a fast changing wireless propagation channel meaning a short coherence time.

Fig. 8. Comparison of wireless propagation channels using the CDF of the spectral efficiency. To analyze the behavior over time, the calculated beamforming matrices were applied over several channel matrices delayed with τ.

general improvement of the eigenvalues or MER occurring over time. To illustrate the loss in spectral efficiency by using a time delayed beamforming matrix, the spectral efficiency is calculated for each channel matrix with delayed versions of the beamforming matrices. This indicates the difference between the time-delayed beamforming matrix and the optimum spectral efficiency, which can be reached at this point in time. Note that the minimum delay time is limited by the OFDM symbol duration $T_\mathrm{o} = 128\,\mu\mathrm{s}$. For a scenario with a long coherence time we selected the measurement point marked as g_9 within Fig. 3. The communication link is dominated by a LOS connection with an average MER of $16.7\,\mathrm{dB}$ and no foliage between the base station and mobile transmitter. The results in Fig. 8(a) show a slow degradation in spectral efficiency with increasing estimation delay. This means the channel is changing slowly over time. Even for a high delay time of $\tau = 16.2\,\mathrm{ms}$ a drop in spectral efficiency of only $1.2\,\mathrm{bps/Hz}$ is reached in $90\,\%$ of the cases. In contrast, the measurement point marked as g_{10} within Fig. 3 is analyzed, showing an average MER of $9.3\,\mathrm{dB}$. Within this propagation scenario the LOS path is covered by dense foliage, which

rapidly changed the channel over time due to motions of leaves from the wind present that day. The difference is visualized in Fig. 8(b). Already after $\tau = 128\,\mu\text{s}$ the wireless propagation channel and thereby the ideal beamforming matrix changed drastically leading to a drop of $8\,\text{bps/Hz}$ in $90\,\%$ of the cases. Nevertheless, a saturation effect is visible caused by the static non-variant parts in the propagation environment.

V. Conclusion

This work presents a measurement-based analysis of the wireless propagation channel around $28\,\text{GHz}$ using a MIMO measurement system. Overall, 159 channel measurements at static mobile transmitter positions have been performed in three realistic small cell site scenarios. The spatial diversity of the channel is analyzed, showing less than $10\,\text{dB}$ attenuation of the second path in $50\,\%$ of the cases, which show the possibility for spatial multiplexing techniques in future mobile communication scenarios at the edge of the mmWave regime. Moreover, the significant influences of moving foliage are investigated and their effects on the achievable spectral efficiency indicate the constraints for data frame durations. The channel sounder enables an estimation of the complex MIMO channel matrix, which can be fed into numerical simulations to investigate MIMO architectures and algorithms.

Acknowledgment

The authors thank A. Lipp, A. Gallego and M. Nonnenmacher for their excellent support in building up the demonstrator.

References

[1] J. G. Andrews, S. Buzzi, W. Choi, S. V. Hanly, A. Lozano, A. C. Soong, and J. C. Zhang, "What will 5G be?" *IEEE Journal on Selected Areas in Communications*, vol. 32, no. 6, pp. 1065–1082, jun 2014.

[2] H. Viswanathan and M. Weldon, "The Past, Present, and Future of Mobile Communications," *Bell Labs Technical Journal*, vol. 19, pp. 8–21, 2014.

[3] A. Swindlehurst, E. Ayanoglu, P. Heydari, and F. Capolino, "Millimeter-wave massive MIMO: The next wireless revolution?" *IEEE Communications Magazine*, vol. 52, no. 9, pp. 56–62, 2014.

[4] A. Goldsmith, S. A. Jafar, N. Jindal, and S. Vishwanath, "Capacity limits of MIMO channels," *IEEE Journal on Selected Areas in Communications*, vol. 21, no. 5, pp. 684–702, 2003.

[5] M. Xiao, S. Mumtaz, Y. Huang, L. Dai, Y. Li, M. Matthaiou, G. K. Karagiannidis, E. Bjornson, K. Yang, C.-L. I, and A. Ghosh, "Millimeter Wave Communications for Future Mobile Networks," *IEEE Journal on Selected Areas in Communications*, vol. 35, no. 9, pp. 1909–1935, sep 2017.

[6] H. Yan, S. Ramesh, T. Gallagher, C. Ling, and D. Cabric, "Performance, Power, and Area Design Trade-Offs in Millimeter-Wave Transmitter Beamforming Architectures," *IEEE Circuits and Systems Magazine*, vol. 19, no. 2, pp. 33–58, 2019.

[7] R. Baldemair, T. Irnich, K. Balachandran, E. Dahlman, G. Mildh, Y. Selén, S. Parkvall, M. Meyer, and A. Osseiran, "Ultra-dense networks in millimeter-wave frequencies," *IEEE Communications Magazine*, vol. 53, no. 1, pp. 202–208, jan 2015.

[8] X. Gao, O. Edfors, F. Rusek, and F. Tufvesson, "Massive MIMO Performance Evaluation Based on Measured Propagation Data," *IEEE Transactions on Wireless Communications*, vol. 14, no. 7, pp. 3899–3911, 2015.

[9] S. A. Busari, K. M. S. Huq, S. Mumtaz, L. Dai, and J. Rodriguez, "Millimeter-Wave Massive MIMO Communication for Future Wireless Systems: A Survey," *IEEE Communications Surveys and Tutorials*, vol. 20, no. 2, pp. 836–869, 2018.

[10] E. Björnson, E. G. Larsson, and T. L. Marzetta, "Massive MIMO: Ten myths and one critical question," *IEEE Communications Magazine*, vol. 54, no. 2, pp. 114–123, feb 2016.

[11] S. Sun, T. S. Rappaport, R. W. Heath, A. Nix, and S. Rangan, "MIMO for millimeter-wave wireless communications: Beamforming, spatial multiplexing, or both?" *IEEE Communications Magazine*, vol. 52, no. 12, pp. 110–121, dec 2014.

[12] *Technical Specification Group Radio Access Network; New frequency range for NR (24.25-29.5 GHz) (Release 15)*, 3rd Generation Partnership Project (3GPP), jun 2018, v1.0.0 (2018-06).

[13] K. Yu and B. Ottersten, "Models for MIMO propagation channels: A review," *Wireless Communications and Mobile Computing*, vol. 2, no. 7, pp. 653–666, nov 2002.

[14] T. S. Rappaport, Y. Xing, G. R. MacCartney, A. F. Molisch, E. Mellios, and J. Zhang, "Overview of Millimeter Wave Communications for Fifth-Generation (5G) Wireless Networks-With a Focus on Propagation Models," *IEEE Transactions on Antennas and Propagation*, vol. 65, no. 12, pp. 6213–6230, 2017.

[15] R. S. Thomä, D. Hampicke, A. Richter, G. Sommerkorn, and U. Trautwein, "MIMO vector channel sounder measurement for smart antenna system evaluation," *European Transactions on Telecommunications*, vol. 12, no. 5, pp. 427–438, sep 2001.

[16] T. S. Rappaport, G. R. MacCartney, M. K. Samimi, and S. Sun, "Wideband millimeter-wave propagation measurements and channel models for future wireless communication system design," *IEEE Transactions on Communications*, vol. 63, no. 9, pp. 3029–3056, sep 2015.

[17] C. U. Bas, R. Wang, S. Sangodoyin, D. Psychoudakis, T. Henige, R. Monroe, J. Park, C. J. Zhang, and A. F. Molisch, "Real-Time Millimeter-Wave MIMO Channel Sounder for Dynamic Directional Measurements," *IEEE Transactions on Vehicular Technology*, vol. 68, no. 9, pp. 8775–8789, sep 2019.

[18] G. R. MacCartney and T. S. Rappaport, "A Flexible Millimeter-Wave Channel Sounder With Absolute Timing," *IEEE Journal on Selected Areas in Communications*, vol. 35, no. 6, pp. 1402–1418, jun 2017.

[19] H. Tataria, E. L. Bengtsson, P. C. Karlsson, O. Edfors, and F. Tufvesson, "Design and Implementation Aspects of a 28 GHz Channel Sounder for Dynamic Propagation Characterization," *European Cooperation in Science and Technology (EURO-COST)*, 2019.

[20] C. Gentile, P. B. Papazian, N. Golmie, K. A. Remley, P. Vouras, J. Senic, J. Wang, D. Caudill, C. Lai, R. Sun, and J. Chuang, "Millimeter-Wave Channel Measurement and Modeling: A NIST Perspective," *IEEE Communications Magazine*, vol. 56, no. 12, pp. 30–37, dec 2018.

[21] S. Hur, Y. J. Cho, J. Lee, N. G. Kang, J. Park, and H. Benn, "Synchronous channel sounder using horn antenna and indoor measurements on 28 GHz," *2014 IEEE International Black Sea Conference on Communications and Networking, BlackSeaCom 2014*, pp. 83–87, 2014.

[22] S. Hur, Y. J. Cho, T. Kim, J. Park, A. F. Molisch, K. Haneda, and M. Peter, "Wideband spatial channel model in an urban cellular environments at 28 GHz," *2015 9th European Conference on Antennas and Propagation, EuCAP 2015*, pp. 1–5, 2015.

[23] S. Hur, S. Baek, B. Kim, Y. Chang, A. F. Molisch, T. S. Rappaport, K. Haneda, and J. Park, "Proposal on Millimeter-Wave Channel Modeling for 5G Cellular System," *IEEE Journal of Selected Topics in Signal Processing*, vol. 10, no. 3, pp. 454–469, apr 2016.

[24] S. Hur, H. Yu, J. Park, W. Roh, C. U. Bas, R. Wang, and A. F. Molisch, "Feasibility of mobility for millimeter-wave systems based on channel measurements," *IEEE Communications Magazine*, vol. 56, no. 7, pp. 56–63, 2018.

[25] Z. Wen, H. Kong, Q. Wang, S. Li, X. Zhao, M. Wang, and S. Sun, "mmWave channel sounder based on COTS instruments for 5G and indoor channel measurement," in *2016 IEEE Wireless Communications and Networking Conference*, vol. 2016-Septe, no. Mwmc5g. IEEE, apr 2016, pp. 1–7.

[26] P. B. Papazian, K. A. Remley, C. Gentile, and N. Golmie, "Radio channel sounders for modeling mobile communications at 28 GHz, 60 GHz and 83 GHz," in *Global Symposium on Millimeter-Waves (GSMM)*, vol. 4. IEEE, may 2015, pp. 1–3.

[27] O. H. Koymen, A. Partyka, S. Subramanian, and J. Li, "Indoor mm-Wave Channel Measurements: Comparative Study of 2.9 GHz and 29 GHz," in *2015 IEEE Global Communications Conference (GLOBECOM)*. IEEE, dec 2015, pp. 1–6.

[28] J. Ryu, A. Partyka, S. Subramanian, and A. Sampath, "Study of the Indoor Millimeter Wavelength Channel," in *2015 IEEE Global Communications Conference (GLOBECOM)*. IEEE, dec 2015, pp. 1–6.

[29] J. Lee, J. Liang, J.-J. Park, and M.-D. Kim, "Directional path loss characteristics of large indoor environments with 28 GHz measurements," in *2015 IEEE 26th Annual International Symposium on Personal, Indoor,*

and Mobile Radio Communications (PIMRC), vol. 2015-Decem. IEEE, aug 2015, pp. 2204–2208.

[30] H.-K. Kwon, M.-D. Kim, and Y.-j. Chong, "Implementation and performance evaluation of mmWave channel sounding system," in *2015 IEEE International Symposium on Antennas and Propagation & USNC/URSI National Radio Science Meeting*, vol. 2015-Octob. IEEE, jul 2015, pp. 1011–1012.

[31] R. Muller, R. Herrmann, D. A. Dupleich, C. Schneider, and R. S. Thoma, "Ultrawideband multichannel sounding for mm-wave," in *The 8th European Conference on Antennas and Propagation (EuCAP 2014)*, vol. 8, no. EuCAP. IEEE, apr 2014, pp. 817–821.

[32] T. Nakamura, A. Benjebbour, Y. Kishiyama, S. Suyama, and T. Imai, "5G Radio Access: Requirements, Concept and Experimental Trials," *IEICE Transactions on Communications*, vol. E98.B, no. 8, pp. 1397–1406, 2015.

[33] X. Yin, C. Ling, and M.-D. Kim, "Experimental Multipath-Cluster Characteristics of 28-GHz Propagation Channel," *IEEE Access*, vol. 3, pp. 3138–3150, 2015.

[34] M. Lei, J. Zhang, T. Lei, and D. Du, "28-GHz indoor channel measurements and analysis of propagation characteristics," in *2014 IEEE 25th Annual International Symposium on Personal, Indoor, and Mobile Radio Communication (PIMRC)*, vol. 2014-June. IEEE, sep 2014, pp. 208–212.

[35] X. Wu, Y. Zhang, C. X. Wang, G. Goussetis, E. H. M. Aggoune, and M. M. Alwakeel, "28 GHz indoor channel measurements and modelling in laboratory environment using directional antennas," *2015 9th European Conference on Antennas and Propagation, EuCAP 2015*, pp. 1–5, 2015.

[36] C. Larsson, F. Harrysson, B.-E. Olsson, and J.-E. Berg, "An outdoor-to-indoor propagation scenario at 28 GHz," in *The 8th European Conference on Antennas and Propagation (EuCAP 2014)*, no. EuCAP. IEEE, apr 2014, pp. 3301–3304.

[37] J. Huang, R. Feng, J. Sun, C.-X. Wang, W. Zhang, and Y. Yang, "Multi-frequency millimeter wave massive MIMO channel measurements and analysis," in *2017 IEEE International Conference on Communications (ICC)*. IEEE, may 2017, pp. 1–6.

[38] M. M. Lodro, N. Majeed, A. A. Khuwaja, A. H. Sodhro, and S. Greedy, "Statistical channel modelling of 5G mmWave MIMO wireless communication," in *2018 International Conference on Computing, Mathematics and Engineering Technologies (iCoMET)*, vol. 2018-Janua. IEEE, mar 2018, pp. 1–5.

[39] J. Hejselbaek, Y. Ji, W. Fan, and G. F. Pedersen, "Channel Sounding System for MM-Wave Bands and Characterization of Indoor Propagation at 28 GHz," *International Journal of Wireless Information Networks*, vol. 24, no. 3, pp. 204–216, sep 2017.

[40] T. Jiang, L. Tian, P. Tang, Z. Hu, and J. Zhang, "Basestation 3-dimensional spatial propagation characteristics in urban microcell at 28 GHz," in *2017 11th European Conference on Antennas and Propagation (EUCAP)*. IEEE, mar 2017, pp. 3167–3171.

[41] L. Zhou, L. Xiao, J. Li, Z. Yang, J. Lian, and S. Zhou, "Path Loss Model Based on Cluster at 28GHz in the Office and Corridor Environments," in *2016 IEEE 84th Vehicular Technology Conference (VTC-Fall)*, vol. 0. IEEE, sep 2016, pp. 1–5.

[42] S. Dahal, M. Faulkner, H. King, and S. Ahmed, "27.1 GHz Millimetre Wave Propagation Measurements for 5G Urban Macro Areas," in *2017 IEEE 85th Vehicular Technology Conference (VTC Spring)*, vol. 2017-June, no. 2. IEEE, jun 2017, pp. 1–5.

[43] P. Zhang, J. Li, H. Wang, and W. Hong, "Measurement-Based Propagation Characteristics at 28 GHz and 39 GHz in Suburban Environment," in *2019 IEEE International Symposium on Antennas and Propagation and USNC-URSI Radio Science Meeting*. IEEE, jul 2019, pp. 2121–2122.

[44] J.-H. Lee, J.-S. Choi, and S.-C. Kim, "Cell Coverage Analysis of 28 GHz Millimeter Wave in Urban Microcell Environment Using 3-D Ray Tracing," *IEEE Transactions on Antennas and Propagation*, vol. 66, no. 3, pp. 1479–1487, mar 2018.

[45] R. Naderpour, J. Vehmas, S. Nguyen, J. Jarvelainen, and K. Haneda, "Spatio-temporal channel sounding in a street canyon at 15, 28 and 60 GHz," in *2016 IEEE 27th Annual International Symposium on Personal, Indoor, and Mobile Radio Communications (PIMRC)*. IEEE, sep 2016, pp. 1–6.

[46] Y. Liu, L. Lin, and R. Zhang, "MIMO channel sounder and millimeter wave measurements in a conference room," in *2016 11th International Symposium on Antennas, Propagation and EM Theory (ISAPE)*. IEEE, oct 2016, pp. 812–814.

[47] G. R. Maccartney, T. S. Rappaport, M. K. Samimi, and S. Sun, "Millimeter-Wave Omnidirectional Path Loss Data for Small Cell 5G Channel Modeling," *IEEE Access*, vol. 3, pp. 1573–1580, 2015.

[48] G. R. Maccartney, M. K. Samimi, and T. S. Rappaport, "Omnidirectional path loss models in New York City at 28 GHz and 73 GHz," in *IEEE International Symposium on Personal, Indoor and Mobile Radio Communications, PIMRC*, vol. 2014-June. IEEE, sep 2014, pp. 227–231.

[49] C. U. Bas, R. Wang, D. Psychoudakis, T. Henige, R. Monroe, J. Park, J. Zhang, and A. F. Molisch, "A real-time millimeter-wave phased array MIMO channel sounder," *IEEE Vehicular Technology Conference*, vol. 2017-September, no. i, pp. 1–6, 2018.

[50] C. Umit Bas, R. Wang, S. Sangodoyin, T. Choi, S. Hur, K. Whang, J. Park, C. J. Zhang, and A. F. Molisch, "Outdoor to Indoor Propagation Channel Measurements at 28 GHz," *IEEE Transactions on Wireless Communications*, vol. 18, no. 3, pp. 1477–1489, mar 2019.

[51] C. U. Bas, R. Wang, T. Choi, S. Hur, K. Whang, J. Park, J. Zhang, and A. F. Molisch, "Outdoor to Indoor Penetration Loss at 28 GHz for Fixed Wireless Access," in *2018 IEEE International Conference on Communications (ICC)*, vol. 2018-May. IEEE, may 2018, pp. 1–6.

[52] C. U. Bas, R. Wang, S. Sangodoyin, S. Hur, K. Whang, J. Park, J. Zhang, and A. F. Molisch, "Dynamic Double Directional Propagation Channel Measurements at 28 GHz - Invited Paper," in *2018 IEEE 87th Vehicular Technology Conference (VTC Spring)*, vol. 2018-June. IEEE, jun 2018, pp. 1–6.

[53] W. Roh, J. Y. Seol, J. H. Park, B. Lee, J. Lee, Y. Kim, J. Cho, K. Cheun, and F. Aryanfar, "Millimeter-wave beamforming as an enabling technology for 5G cellular communications: Theoretical feasibility and prototype results," *IEEE Communications Magazine*, vol. 52, no. 2, pp. 106–113, feb 2014.

[54] Y. Kim, H. Y. Lee, P. Hwang, R. K. Patro, J. Lee, W. Roh, and K. Cheun, "Feasibility of Mobile Cellular Communications at Millimeter Wave Frequency," *IEEE Journal on Selected Topics in Signal Processing*, vol. 10, no. 3, pp. 589–599, apr 2016.

[55] B. Yang, Z. Yu, J. Lan, R. Zhang, J. Zhou, and W. Hong, "Digital Beamforming-Based Massive MIMO Transceiver for 5G Millimeter-Wave Communications," *IEEE Transactions on Microwave Theory and Techniques*, vol. 66, no. 7, pp. 3403–3418, jul 2018.

[56] T. Obara, Y. Inoue, Y. Aoki, S. Suyama, J. Lee, and Y. Okumurav, "Experiment of 28 GHz Band 5G super wideband transmission using beamforming and beam tracking in high mobility environment," *IEEE International Symposium on Personal, Indoor and Mobile Radio Communications, PIMRC*, pp. 1–5, 2016.

[57] J. Mashino, K. Satoh, S. Suyama, Y. Inoue, and Y. Okumura, "5G Experimental Trial of 28 GHz Band Super Wideband Transmission Using Beam Tracking in Super High Mobility Environment," *IEEE Vehicular Technology Conference*, vol. 2017-June, 2017.

[58] D. Kurita, K. Tateishi, A. Harada, Y. Kishiyama, S. Itoh, H. Murai, A. Simonsson, and P. Ökvist, "Outdoor experiments on 5G radio access using distributed MIMO and beamforming in 28-GHz Frequency Band," *IEEE International Symposium on Personal, Indoor and Mobile Radio Communications, PIMRC*, vol. 2017-October, pp. 1–6, 2018.

[59] J. Proakis and M. Salehi, *Digital Communications 5th Edition*. McGraw Hill Higher Education, 2008.

[60] A. Alkhateeb, G. Leus, and R. W. Heath, "Limited Feedback Hybrid Precoding for Multi-User Millimeter Wave Systems," *IEEE Transactions on Wireless Communications*, vol. 14, no. 11, pp. 6481–6494, 2015.

[61] X. Gao, L. Dai, S. Han, I. Chih-Lin, and R. W. Heath, "Energy-Efficient Hybrid Analog and Digital Precoding for MmWave MIMO Systems with Large Antenna Arrays," *IEEE Journal on Selected Areas in Communications*, vol. 34, no. 4, pp. 998–1009, apr 2016.

[62] N. N. Moghadam, G. Fodor, M. Bengtsson, and D. J. Love, "On the energy efficiency of MIMO hybrid beamforming for millimeter-wave systems with nonlinear power amplifiers," *IEEE Transactions on Wireless Communications*, vol. 17, no. 11, pp. 7208–7221, nov 2018.

[63] D. Zhang, Y. Wang, X. Li, and W. Xiang, "Hybridly Connected Structure for Hybrid Beamforming in mmWave Massive MIMO Systems," *IEEE Transactions on Communications*, vol. 66, no. 2, pp. 662–674, feb 2018.

[64] J. Eisenbeis, T. Mahler, P. R. López, and T. Zwick, "Channel estimation method for subarray based hybrid beamforming systems employing sparse arrays," *Progress In Electromagnetics Research C*, vol. 87, pp. 25–38, 2018.

[65] Lang Tong, B. Sadler, and Min Dong, "Pilot-assisted wireless transmissions - General model, design criteria, and signal processing," *IEEE Signal Processing Magazine*, vol. 21, no. 6, pp. 12–25, nov 2004.

[66] T. Zwick, T. J. Beukema, and H. Nam, "Wideband channel sounder with measurements and model for the 60 GHz indoor radio channel," *IEEE*

Transactions on Vehicular Technology, vol. 54, no. 4, pp. 1266–1277, 2005.
[67] T. Mahler, J. Kowalewski, B. Nuß, C. Richt, J. Mayer, and T. Zwick, "Channel measurement based antenna synthesis for mobile automotive MIMO communication systems," *Progress In Electromagnetics Research B*, vol. 72, no. 1, pp. 1–16, 2017.
[68] B. Sklar, "Rayleigh fading channels in mobile digital communication systems .II. Mitigation," *IEEE Communications Magazine*, vol. 35, no. 7, pp. 102–109, jul 1997.
[69] M. Morelli, C.-C. J. Kuo, and M.-O. Pun, "Synchronization Techniques for Orthogonal Frequency Division Multiple Access (OFDMA): A Tutorial Review," *Proceedings of the IEEE*, vol. 95, no. 7, pp. 1394–1427, jul 2007.
[70] M. Raghavendra and K. Giridhar, "Improving channel estimation in OFDM systems for sparse multipath channels," *IEEE Signal Processing Letters*, vol. 12, no. 1, pp. 52–55, jan 2005.
[71] O. Edfors, M. Sandell, J.-J. van de Beek, S. Wilson, and P. Ola Borjesson, "OFDM channel estimation by singular value decomposition," in *Proceedings of Vehicular Technology Conference - VTC*, vol. 2. IEEE, 1996, pp. 923–927.
[72] T. Hwang, C. Yang, G. Wu, S. Li, and G. Ye Li, "OFDM and Its Wireless Applications: A Survey," *IEEE Transactions on Vehicular Technology*, vol. 58, no. 4, pp. 1673–1694, may 2009.
[73] H. Arslan and G. E. Bottomley, "Channel estimation in narrowband wireless communication systems," *Wireless Communications and Mobile Computing*, vol. 1, no. 2, pp. 201–219, 2001.
[74] *Digital Video Broadcasting (DVB); Measurement guidelines for DVB systems*, European Telecommunications Standards Institute (ETSI), may 2001, v1.2.1 (2001-05), Reference: RTR/JTC-DVB-77.
[75] S. Loyka and G. Levin, "On physically-based normalization of MIMO channel matrices," *IEEE Transactions on Wireless Communications*, vol. 8, no. 3, pp. 1107–1112, 2009.
[76] *Technical Specification Group Radio Access Network; Study on 3D channel model for LTE (Release 12)*, 3rd Generation Partnership Project (3GPP), dec 2014, v12.7.0 (2017-12).
[77] T. S. Rappaport, S. Sun, R. Mayzus, H. Zhao, Y. Azar, K. Wang, G. N. Wong, J. K. Schulz, M. Samimi, and F. Gutierrez, "Millimeter wave mobile communications for 5G cellular: It will work!" *IEEE Access*, vol. 1, pp. 335–349, 2013.
[78] Y. Azar, G. N. Wong, K. Wang, R. Mayzus, J. K. Schulz, H. Zhao, F. Gutierrez, D. Hwang, and T. S. Rappaport, "28 GHz propagation measurements for outdoor cellular communications using steerable beam antennas in New York city," in *IEEE International Conference on Communications*. IEEE, jun 2013, pp. 5143–5147.

Joerg Eisenbeis (S'16) received his B.Sc. and M.Sc. degrees in electrical engineering and information technology from the Karlsruhe Institute of Technology (KIT), Germany, in 2012 and 2014, respectively. For his Master's thesis entitled "*Systemsimulationen von Breitbandkommunikationssystemen im E-Band*", he received the *TESAT RAUMFAHRTPREIS* 2015 awarded by the German Association for Aerospace. Since 2015 he is a research associate and working toward the Dr.-Ing. (Ph.D.E.E.) degree at the Institute of Radio Frequency Engineering and Electronics, KIT. His research focuses on mobile wireless communication systems.

Magnus Tingulstad received his B.Sc. from RWTH Aachen University, Germany, in 2017 and his M.Sc. from Karlsruhe Institute of Technology, Germany, in 2019. He currently works for the Norwegian telecommunications company Telenor ASA.

Nicolai Kern (S'19) received the M.Sc. degree in electrical engineering from the Karlsruhe Institute of Technology, Karlsruhe, Germany, in 2019. He is currently pursuing the Ph.D. degree at the Institute of Microwave Engineering, Ulm University, Ulm, Germany. His research interests include machine learning applications in radar and radar sensor network signal processing.

Zsolt Kollár (S'11-M'17) received his diploma and Ph.D. degree in electric engineering from the Budapest University of Technology and Economics, Hungary, in 2008 and 2013, respectively. He is an associate professor in the Department of Broadband Infocommunications and Electromagnetic Theory at the Budapest University of Technology and Economics, Hungary, where he is the head of the MATLAB laboratory. He was a visiting researcher at KIT between October 2018 and April 2019. His research interests are digital signal processing, wireless communication, and quantization issues.

Jerzy Kowalewski (S'13) received the B.Sc. degree from Gdansk University of Technology, Gdansk, Poland, in 2011, and the M.Sc. degree in electrical engineering from Karlsruhe Institute of Technology (KIT), Karlsruhe, Germany, in 2013. He is currently working toward the Dr.-Ing. (Ph.D.E.E.) degree at the Institute of Radio Frequency Engineering and Electronics, Karlsruhe Institute of Technology (KIT). His main research topic is reconfigurable antennas with the focus on pattern reconfiguration. His further interest are antennas for communication applications, UWB antennas and wireless propagation topics.

Pablo Ramos López received his B.Sc. degree in electrical engineering and information technology from the Karlsruhe Institute of Technology (KIT), Germany, in 2018. From June 2018 to August 2019 he worked as a student research assistant at the Institute of Radio Frequency Engineering and Electronics (IHE), KIT. Currently he is a graduate student at the department of Electrical Engineering and Information Technology at KIT.

Thomas Zwick (S'95–M'00–SM'06–F'18) received the Dipl.-Ing. and the Dr.-Ing. degrees from the Universität Karlsruhe (TH), Germany, in 1994 and 1999, respectively. In February 2001, he joined IBM as research staff member at the IBM T. J. Watson Research Center, Yorktown Heights, NY, USA. From October 2004 to September 2007, Thomas Zwick was with Siemens AG, Lindau, Germany, managing the RF development team for automotive radars. In October 2007, he became a full professor at the Karlsruhe Institute of Technology (KIT), Germany. He is the director of the Institute of Radio Frequency Engineering and Electronics at the KIT.